

# Supplemental Material on “Topology shapes dynamics on higher-order networks”

Ana P. Millán<sup>1</sup>, Hanlin Sun<sup>2</sup>, Lorenzo Giambagli<sup>3,4</sup>, Riccardo Muolo<sup>5</sup>, Timoteo Carletti<sup>3</sup>, Joaquín J. Torres<sup>1</sup>, Filippo Radicchi<sup>6</sup>, Jürgen Kurths<sup>7,8</sup>, Ginestra Bianconi<sup>9,10,11</sup>

<sup>11</sup> *Institute “Carlos I” for Theoretical and Computational Physics,  
and Electromagnetism and Matter Physics Department,  
University of Granada, E-18071 Granada, Spain*

<sup>2</sup> *Nordita, KTH Royal Institute of Technology and Stockholm University,  
Hannes Alfvéns väg 12, SE-106 91 Stockholm, Sweden*

<sup>3</sup> *Department of Mathematics & naXys, Namur Institute for Complex Systems,  
University of Namur, Rue Grafé 2, B5000 Namur, Belgium*

<sup>4</sup> *Department of Physics and Astronomy, University of Florence, INFN & CSDC, Sesto Fiorentino, Italy*

<sup>5</sup> *Department of Systems and Control Engineering, Tokyo Institute of Technology  
2 Chome-12-1 Ookayama, Meguro-ku, Tokyo, 152-8552, Japan*

<sup>6</sup> *Center for Complex Networks and Systems Research, Luddy School of Informatics,  
Computing, and Engineering, Indiana University, Bloomington, 47408, USA*

<sup>7</sup> *Potsdam Institute for Climate Impact Research, Potsdam, Germany*

<sup>8</sup> *Department of Physics, Humboldt University of Berlin, Berlin, Germany*

<sup>9</sup> *School of Mathematical Sciences, Queen Mary University of London, London E1 4NS, United Kingdom*

<sup>10</sup> *The Alan Turing Institute, The British Library,  
6 Euston Road, London, NW1 2DB, United Kingdom*

We provide background information on Topology and Dynamics of higher-order networks and we provide details about the figures of the main text, the Supplementary Videos and the Supporting Codes.

## I. SIMPLICIAL COMPLEXES AND FUNDAMENTAL OPERATORS IN ALGEBRAIC TOPOLOGY

In this section we provide a very brief introduction to simplicial complexes and algebraic topology operators. The reader who wants to deepen their understanding of the field can consider the following bibliography [1–3].

### A. Definition of simplicial complexes

A  $n$ -dimensional simplex  $\alpha$  (also indicated as a  $n$ -simplex  $\alpha$ ) is formed by a set of  $(n + 1)$  interacting nodes  $v_r$  with  $0 \leq r \leq n$ , i.e.

$$\alpha = [v_0, v_1, v_2 \dots, v_n].$$

A simplex indicates a higher-order interaction in a complex system and admits a topological and geometrical interpretation. For instance a 0-simplex is a node, a 1-simplex is a edge and a 2-simplex is a triangle. A face of a  $n$ -dimensional simplex  $\alpha$  is a simplex  $\alpha'$  formed by a proper subset of nodes of the simplex, i.e.,  $\alpha' \subset \alpha$ . Thus a 2-simplex  $\alpha = [1, 2, 3]$  admits as faces three edges  $([1, 2], [2, 3], [1, 3])$  and three nodes  $([1], [2], [3])$ . A simplicial complex  $\mathcal{K}$  is a set of simplices closed under the inclusion of the faces. Therefore if a triangle is included in the simplicial complex, then all its edges and all its nodes will belong to the simplicial complex as well.

In the following we indicate with  $N_n$  the number of  $n$ -dimensional simplices in the simplicial complex. The dimension  $d$  of the simplicial complex is the maximum dimension of its simplices.

In algebraic topology simplices are oriented, and in most of the cases the orientation is induced by the node labels. For instance a edge  $[i, j]$  is oriented positively if  $i < j$ , similarly a triangle  $[i, j, k]$  is oriented positively if  $i < j < k$  and for any even permutation of the labels of the nodes.

Note that a simplicial complex has a natural weighted extension [4, 5].

### B. The Boundary and Coboundary operators

Topological signals are dynamical variables that are associated not only to nodes, but also to edges, and higher-dimensional simplices of a simplicial complex. Topological signals defined on  $n$ -dimensional simplices are cochains

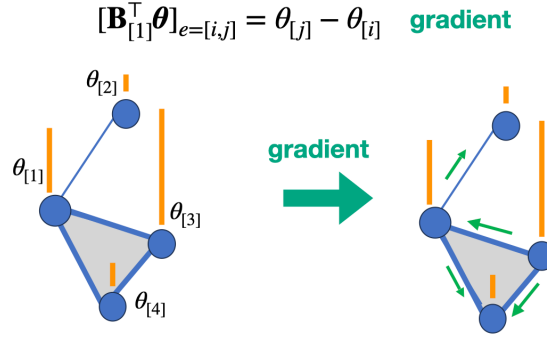


FIG. S-1. **Schematic description of the coboundary matrix  $\mathbf{B}_{[1]}^\top$ .** The coboundary matrix  $\mathbf{B}_{[1]}^\top$  implements the discrete gradient.

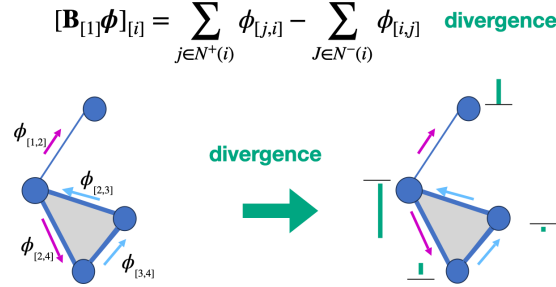


FIG. S-2. **Schematic description of the boundary matrix  $\mathbf{B}_{[1]}$ .** The boundary matrix  $\mathbf{B}_{[1]}$  implements the discrete divergence.

$\chi \in C^n$ , where  $\chi$  has elements specifying the value of the cochain on each  $n$ -simplex of the simplicial complex.

The *coboundary operator*  $\delta_0 : C^0 \rightarrow C^1$  maps 0-cochains (functions defined on nodes) onto 1-cochains and acts as the gradient. This coboundary operator is encoded into the  $N_1 \times N_0$  coboundary matrix  $\mathbf{B}_{[1]}^\top$  such that if  $\theta \in C^0$

$$[\mathbf{B}_{[1]}^\top \theta]_{[i,j]} = \theta_{[j]} - \theta_{[i]}. \quad (\text{S-1})$$

This expression clearly indicates that the node topological signal is mapped into a edge topological signal where each edge is associated to the discrete gradient of the function on its two end-nodes (see Figure S – 1). The *boundary operator*  $\delta_0^* : C^1 \rightarrow C^0$  is the adjoint operator of  $\delta_0$  according to the  $L^2$  norm among cochains. It maps 1-cochains into 0-cochains and defines the discrete divergence of the edge topological signals. The boundary operator is encoded into the  $N_0 \times N_1$  matrix  $\mathbf{B}_{[1]}$ , whose action on a 1-cochain  $\phi \in C^1$  obeys

$$[\mathbf{B}_{[1]} \phi]_{[i]} = \sum_{j \in N^+(i)} \phi_{[j,i]} - \sum_{j \in N^-(i)} \phi_{[i,j]}, \quad (\text{S-2})$$

where  $N^+(i)$  indicates the nodes with labels  $j < i$  and  $N^-(i)$  indicates the nodes with labels  $j > i$ . Thus the boundary operators assigns to each node  $i$  the divergence of the signal (flux-in minus flux-out). For a schematic description see Figure S – 2. The boundary and coboundary operators can be extended to higher dimension. For instance the coboundary operator  $\delta_1 : C^1 \rightarrow C^2$  indicates the *curl*. Specifically this operator can be encoded into a  $N_2 \times N_1$  matrix  $\mathbf{B}_{[2]}^\top$  that acts on 1-cochains  $\phi$  as follows:

$$[\mathbf{B}_{[2]}^\top \phi]_{[i,j,k]} = \phi_{[i,j]} + \phi_{[j,k]} - \phi_{[i,k]}. \quad (\text{S-3})$$

From this expression one notices that this operators performs the circulation of the edge signal and associates it to the triangle and can be thus interpreted as the discrete curl. For a schematic representation see Figure S – 3. A fundamental property of the boundary operators is that

$$\mathbf{B}_{[n]} \mathbf{B}_{[n+1]} = \mathbf{0}, \quad \mathbf{B}_{[n+1]}^\top \mathbf{B}_{[n]}^\top = \mathbf{0}, \quad (\text{S-4})$$

valid for any  $n > 0$ , which indicates that the *boundary of a boundary is null*.

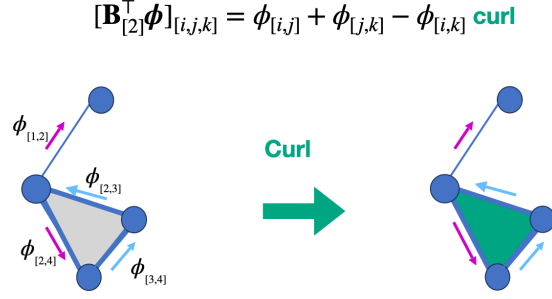


FIG. S-3. **Schematic description of the coboundary matrix  $\mathbf{B}_{[2]}^\top$ .** The coboundary matrix  $\mathbf{B}_{[2]}^\top$  implements the discrete curl.

### C. The Hodge Laplacians

The Hodge Laplacians  $\mathbf{L}_{[n]}$  describes the diffusion from  $n$ -simplices to  $n$ -simplices either going through the  $(n-1)$ -simplices or through the  $(n+1)$ -simplices. It is a  $N_n \times N_n$  matrix obtained by multiplying the boundary matrices as follows:

$$\mathbf{L}_{[n]} = \mathbf{B}_{[n]}^\top \mathbf{B}_{[n]} + \mathbf{B}_{[n+1]} \mathbf{B}_{[n+1]}^\top, \quad (\text{S-5})$$

where  $\mathbf{B}_{[0]} = \mathbf{0}$ . Note that the 0-Hodge Laplacian  $\mathbf{L}_{[0]}$  coincides with the graph Laplacian.

One of the most celebrated properties of the Hodge Laplacians that relates their spectrum with the topology of the simplicial complex is that the dimension of the kernel of the  $n$ -Laplacian  $\mathbf{L}_{[n]}$  is equal to the  $n$ -th Betti number, i.e.

$$\dim \ker(\mathbf{L}_{[n]}) = \beta_n. \quad (\text{S-6})$$

For instance the 1-Hodge Laplacian has a kernel of dimension given by  $\beta_1$  indicating the number of independent cycles of the simplicial complex.

We distinguish between the up and down  $n$ -Hodge Laplacians given by

$$\begin{aligned} \mathbf{L}_{[n]}^{up} &= \mathbf{B}_{[n+1]} \mathbf{B}_{[n+1]}^\top, \\ \mathbf{L}_{[n]}^{down} &= \mathbf{B}_{[n]}^\top \mathbf{B}_{[n]}. \end{aligned} \quad (\text{S-7})$$

The up  $n$ -Laplacian  $\mathbf{L}_{[n]}^{up}$  describes diffusion from  $n$  simplices to  $n$ -simplices going through  $(n-1)$ -simplices, while the down  $n$ -Laplacian  $\mathbf{L}_{[n]}^{down}$  describes diffusion from  $n$ -simplices to  $n$ -simplices going through  $(n+1)$ -simplices. Since the boundary matrices obey Eq.(S-4) it is easy to show that  $\mathbf{L}_{[n]}^{up} \mathbf{L}_{[n]}^{down} = \mathbf{L}_{[n]}^{down} \mathbf{L}_{[n]}^{up} = \mathbf{0}$  which implies that

$$\begin{aligned} \text{im}(\mathbf{L}_{[n]}^{down}) &\subseteq \ker(\mathbf{L}_{[n]}^{up}), \\ \text{im}(\mathbf{L}_{[n]}^{up}) &\subseteq \ker(\mathbf{L}_{[n]}^{down}). \end{aligned} \quad (\text{S-8})$$

This property implies *Hodge decomposition*, indicating that a  $n$ -cochain  $\phi$  can be decomposed uniquely into the sum of an irrotational, a solenoidal and a harmonic component, i.e.,

$$\phi = \phi^{irr} + \phi^{sol} + \phi^{harm}, \quad (\text{S-9})$$

such that  $\mathbf{L}_{[n]}^{up} \phi^{irr} = \mathbf{0}$ ,  $\mathbf{L}_{[n]}^{down} \phi^{sol} = \mathbf{0}$ ,  $\mathbf{L}_{[n]} \phi^{harm} = \mathbf{0}$ .

### D. The Dirac operator

While the Hodge Laplacian only couples topological signals of a given dimension, the discrete Dirac operator [6–8] has the ability to couple signals of different dimensions. It can then be used widely to allow topological signals of different dimensions to cross-talk.

On a simplicial complex of dimension  $d = 2$ , formed by nodes, edges and triangles, the topological Dirac operator  $\mathbf{D} : C^0 \oplus C^1 \oplus C^2 \rightarrow C^0 \oplus C^1 \oplus C^2$  is given by

$$\mathbf{D} = \begin{pmatrix} 0 & \mathbf{B}_{[1]} & 0 \\ \mathbf{B}_{[1]}^\top & 0 & \mathbf{B}_{[2]} \\ 0 & \mathbf{B}_{[2]}^\top & 0 \end{pmatrix}. \quad (\text{S-10})$$

This operator has the property that its square is given by the Gauss-Bonnet Laplacian matrix  $\mathcal{L}$ , i.e.,

$$\mathbf{D}^2 = \mathcal{L} = \begin{pmatrix} \mathbf{L}_{[0]} & 0 & 0 \\ 0 & \mathbf{L}_{[1]} & 0 \\ 0 & 0 & \mathbf{L}_{[2]} \end{pmatrix}. \quad (\text{S-11})$$

Thus the Dirac operator can be understood as the *square root* of the Gauss-Bonnet Laplacian.

An important property of the Dirac operator is that it anti-commutes with the gamma matrix  $\gamma$ , i.e.,

$$\{\mathbf{D}, \gamma\} = \mathbf{D}\gamma + \gamma\mathbf{D} = \mathbf{0}, \quad (\text{S-12})$$

where

$$\gamma = \begin{pmatrix} \mathbf{I}_{N_0} & 0 & 0 \\ 0 & -\mathbf{I}_{N_1} & 0 \\ 0 & 0 & \mathbf{I}_{N_2} \end{pmatrix}. \quad (\text{S-13})$$

This implies that if the topological spinor  $\Psi = (\theta, \phi, \xi)^\top$  is an eigenvector of the Dirac operator with eigenvalue  $\lambda \neq 0$ , then the topological spinor  $\gamma\Psi = (\theta, -\phi, \xi)^\top$  is an eigenvector of the Dirac operator with eigenvalue  $-\lambda$ . In this case we say that the eigenvectors  $\Psi$  and  $\gamma\Psi$  are *chiral*. Note however that harmonic modes of the discrete Dirac operator defined here break chirality.

The Dirac operator obeys *Dirac decomposition*. In order to see this, let us first observe that the Dirac operator can be written as  $\mathbf{D} = \mathbf{D}_{[1]} + \mathbf{D}_{[2]}$  with

$$\mathbf{D}_{[1]} = \begin{pmatrix} 0 & \mathbf{B}_{[1]} & 0 \\ \mathbf{B}_{[1]}^\top & 0 & 0 \\ 0 & 0 & 0 \end{pmatrix}, \quad \mathbf{D}_{[2]} = \begin{pmatrix} 0 & 0 & 0 \\ 0 & 0 & \mathbf{B}_{[2]} \\ 0 & \mathbf{B}_{[2]}^\top & 0 \end{pmatrix}. \quad (\text{S-14})$$

Due to the property Eq.(S-4) of the boundary operator we have

$$\mathbf{D}_{[1]}\mathbf{D}_{[2]} = \mathbf{D}_{[2]}\mathbf{D}_{[1]} = \mathbf{0}, \quad (\text{S-15})$$

thus

$$\begin{aligned} \text{im}(\mathbf{D}_{[1]}) &\subseteq \ker(\mathbf{D}_{[2]}), \\ \text{im}(\mathbf{D}_{[2]}) &\subseteq \ker(\mathbf{D}_{[1]}). \end{aligned} \quad (\text{S-16})$$

This property implies *Dirac decomposition*, indicating that a topological spinor  $\Psi$  can be decomposed uniquely into the sum

$$\Psi = \Psi^{[1]} + \Psi^{[2]} + \Psi^{\text{harm}}. \quad (\text{S-17})$$

such that  $\mathbf{D}_{[2]}\Psi^{[1]} = \mathbf{0}, \mathbf{D}_{[1]}\Psi^{[2]} = \mathbf{0}, \mathbf{D}\Psi^{\text{harm}} = \mathbf{0}$ .

Since we have

$$\mathbf{D}_{[1]}^2 = \begin{pmatrix} \mathbf{L}_{[0]} & 0 & 0 \\ 0 & \mathbf{L}_{[1]}^{\text{down}} & 0 \\ 0 & 0 & 0 \end{pmatrix}, \quad (\text{S-18})$$

given that  $\mathbf{L}_{[0]} = \mathbf{B}_{[1]}\mathbf{B}_{[1]}^\top$  has the same non-zero spectrum of  $\mathbf{L}_{[1]}^{\text{down}} = \mathbf{B}_{[1]}^\top\mathbf{B}_{[1]}$ , it follows that the eigenvalues  $\lambda$  of  $\mathbf{D}_{[1]}$  are given by

$$\lambda = \pm\sqrt{\mu} \quad (\text{S-19})$$

where  $\mu$  are the non zero eigenvalues of the Laplacian  $\mathbf{L}_{[0]}$ . Similarly it can be shown that the non-zero eigenvalues of  $\mathbf{D}_{[2]}$  obey Eq.(S-19) where  $\mu$  are the non-zero eigenvalues of  $\mathbf{L}_{[1]}^{\text{up}}$ .

The Dirac operator admits generalization to weighted simplicial complexes [5], to multiplex networks [9], and to treating multi-dimensional simplicial complexes on nodes and edges [10].

### E. Extension to cell complexes

Simplicial complexes have the restriction that they are only formed by simplices. In order to treat more general structures *cell complexes* are introduced. Cell complexes admit as building blocks any *cell* given by a regular polytope. These include for instance simplices, hypercubes, orthoplex, as long as the cells are glued to each other along faces.

An example of a cell complex is a 2-dimensional square lattice where the squares are taken to be 2-dimensional cells or a 3-dimensional cubic lattice where squares and cubes are taken to be as 2-dimensional and 3-dimensional cells respectively.

The algebraic topology operators introduced before can be all extended to treat cell complexes. In particular we can define boundary and coboundary operators, Hodge Laplacians and Dirac operators for cell complexes as well.

Here and in the following we will discuss the results for simplicial complexes. If not explicitly stated the results valid for cell complexes are a direct extension of the results valid for simplicial complexes.

## II. TOPOLOGICAL DIFFUSION AND SYNCHRONIZATION

### A. Topological diffusion dynamics

Topological diffusion is arguably the simplest example of topological dynamics and has been studied by different authors [11–13].

Topological diffusion is driven by the Hodge Laplacian  $\mathbf{L}_{[n]}$  and for a  $n$ -dimensional topological signal  $\phi \in C^n$  obeys

$$\frac{d\phi}{dt} = -\mathbf{L}_{[n]}\phi. \quad (\text{S-20})$$

Thanks to Hodge decomposition expressed by Eq.(S-9), this dynamics can be expressed in terms of decoupled dynamics for the irrotational, the solenoidal and the harmonic component of the signals

$$\frac{d\phi^{irr}}{dt} = -\mathbf{L}_{[n]}^{down}\phi^{irr}, \quad \frac{d\phi^{sol}}{dt} = -\mathbf{L}_{[n]}^{up}\phi^{sol}, \quad \frac{d\phi^{harm}}{dt} = 0. \quad (\text{S-21})$$

The harmonic component of the signal does not change in time, while the irrotational and the solenoidal components are suppressed in time. Note that for  $n$ -dimensional topological signal the harmonic component has a dimension given by the  $n$ -th Betti number  $\beta_n$  and the harmonic eigenvectors in general are not constant. Thus the scenario is different with respect to the graph case. On one side, a non-trivial steady state is only guaranteed if  $\beta_n > 0$ , on the other side, if  $\beta_n > 0$  the steady state can be non-homogeneous and degenerate for  $\beta_n > 1$  (i.e. dependent on the initial conditions). Note that the harmonic eigenvectors can be chosen to be localized around independent holes of the simplicial complex. It follows that the steady state solution can converge to these harmonic eigenvectors, i.e., learning and identifying the topology of the simplicial complex. Note that for topological diffusion the stationary state is static.

In presence of a non vanishing spectral gap of the Hodge Laplacians  $\mathbf{L}_{[n]}^{down}$  and  $\mathbf{L}_{[n]}^{up}$ , the relaxation dynamics is exponential. Note however that for geometrical networks in which the spectral gap closes, the Hodge Laplacians can display a spectral dimension, and the dynamics can display a power-law temporal relaxation to the steady state [12].

### B. Topological Kuramoto model

Topological diffusion describes a relaxation dynamics toward a constant steady state aligned along the harmonic eigenvectors of the simplicial complex. However, in many real contexts such as in brain dynamics, it is important to describe a coherent dynamical collective dynamics. This leads to the formulation of topological synchronization. The Topological Kuramoto model is a model for non-identical topological oscillators placed on  $n$ -dimensional simplices and captured by the cochain  $\phi \in C^n$  which obeys:

$$\frac{d\phi}{dt} = \omega - \sigma \mathbf{B}_{[n]}^\top \sin(\mathbf{B}_{[n]}\phi) - \sigma \mathbf{B}_{[n+1]} \sin(\mathbf{B}_{[n+1]}^\top \phi). \quad (\text{S-22})$$

Here the sine function is taken element-wise,  $\mathbf{B}_{[n]}$  are the boundary matrices,  $\sigma$  is the coupling constant and  $\omega$  is the vector of intrinsic frequencies drawn typically from a random unimodal distribution, such as a Gaussian or Lorentzian distribution. Note that the Topological Kuramoto model reduces for  $n = 0$  to the standard node based Kuramoto

model[14]. We can define the projected topological signals  $\phi^{[-]}$ ,  $\phi^{[+]}$  defined respectively on  $(n-1)$  and  $(n+1)$  dimensional simplices and defined as:

$$\phi^{[-]} = \mathbf{B}_{[n]}\phi = \mathbf{B}_{[n]}\phi^{irr}, \quad \phi^{[+]} = \mathbf{B}_{[n+1]}^\top\phi = \mathbf{B}_{[n+1]}^\top\phi^{sol}, \quad (\text{S-23})$$

where  $\phi^{[-]}$  depends only on the irrotational component  $\phi^{irr}$  of the topological signal, while  $\phi^{[+]}$  depends only on the solenoidal component  $\phi^{sol}$ . The Topological Kuramoto model decouples into three distinct dynamics for  $\phi^{[-]}$ ,  $\phi^{[+]}$ , and  $\phi^{harm}$ :

$$\begin{aligned} \frac{d\phi^{[-]}}{dt} &= \mathbf{B}_{[n]}\omega - \sigma \mathbf{L}_{[n-1]}^{up} \sin(\phi^{[-]}) , \\ \frac{d\phi^{[+]}}{dt} &= \mathbf{B}_{[n+1]}^\top\omega - \sigma \mathbf{L}_{[n+1]}^{down} \sin(\phi^{[+]}) , \\ \frac{d\phi^{harm}}{dt} &= \omega^{harm} , \end{aligned} \quad (\text{S-24})$$

where  $\omega^{harm}$  is the harmonic component of  $\omega$ .

It follows that in the Topological Kuramoto model the harmonic component of the signal oscillates freely, along the harmonic eigenvectors of the simplicial complexes, typically localized around  $n$ -dimensional holes. The irrotational and solenoidal component of the signal, however, might reach a steady state eventually for large coupling constant  $\sigma$ .

As the coupling constant is raised, then the irrotational and solenoidal components will freeze leaving the harmonic solenoidal dynamics unscreened by the other modes.

It is interesting to observe that the Topological Kuramoto model can be seen [15] as a gradient flow

$$\frac{d\phi}{dt} = -\frac{\partial \mathcal{H}}{\partial \phi} \quad (\text{S-25})$$

with Hamiltonian

$$\mathcal{H} = -\omega^\top \phi - \sigma \mathbf{1}_{N_{n-1}}^\top \cos(\mathbf{B}_{[n]}\phi) - \sigma \mathbf{1}_{N_{n+1}}^\top \cos(\mathbf{B}_{[n+1]}^\top\phi), \quad (\text{S-26})$$

where  $\mathbf{1}_{N_n}$  is the  $N_n$  column vector whose elements are all ones. Note that this Hamiltonian provides the higher-order generalization of the  $n=0$  Hamiltonian for the standard Kuramoto model which is known to have the same interaction term of the XY model [16]. The Topological Kuramoto model admits two complex order parameters depending on  $\phi^{[-]}$  and  $\phi^{[+]}$  respectively:

$$X^{[-]} = \frac{1}{N_{n-1}} \sum_{\alpha} e^{i\phi_{\alpha}^{[-]}}, \quad X^{[+]} = \frac{1}{N_{n+1}} \sum_{\alpha} e^{i\phi_{\alpha}^{[+]}} , \quad (\text{S-27})$$

and two real order parameters  $R^{[\pm]} = |X^{[\pm]}|$ . In terms of these order parameters the Hamiltonian reads

$$\mathcal{H} = -\omega^\top \phi - \sigma N_{n-1} \text{Re} X^{[-]} - \sigma N_{n+1} \text{Re} X^{[+]}. \quad (\text{S-28})$$

Note that these order parameters are only describing to which extent the irrotational and the solenoidal component of the topological signal is frozen, and are not sensitive to the synchronized harmonic dynamics. From the study of these order parameters it emerges that the Topological Kuramoto model continuously synchronizes at zero coupling  $\sigma$ .

The model admits a generalization leading to the Explosive Topological Kuramoto model with a discontinuous synchronization transition occurring at non-zero coupling. The Explosive Topological Kuramoto model [17, 18] is obtained by introducing a global adaptive coupling of the coupling constant. Thus the dynamics obeys:

$$\frac{d\phi}{dt} = \omega - \sigma R^{[+]} \mathbf{B}_{[n]}^\top \sin(\mathbf{B}_{[n]}\phi) - \sigma R^{[-]} \mathbf{B}_{[n+1]} \sin(\mathbf{B}_{[n+1]}^\top\phi) . \quad (\text{S-29})$$

This dynamics simulated on a random graph can be solved within the annealed approximation leading to a theoretical derivation of the discontinuous synchronization transition in excellent agreement with simulation results [18]. The Topological Kuramoto model can be extended to weighted and directed simplicial complexes [15, 19? ].

### C. Global Topological Synchronization

Topological signals can also undergo Global Topological Synchronization [20], although this dynamical state can only be allowed for specific topologies. We consider the case of identical topological oscillators captured by the  $n$ -order topological signal  $\phi$  with elements  $\phi_\alpha \in \mathbb{R}^m$ . The Global Topological Synchronization obeys the dynamics

$$\frac{d\phi}{dt} = F(\phi) - \sigma \mathbf{L}_{[n]} h(\phi) . \quad (\text{S-30})$$

where the functions  $F$  and  $h$  are taken element-wise with  $F(\phi_\alpha) \in \mathbb{R}^m$  and  $h(\phi_\alpha) \in \mathbb{R}^m$ ,  $\mathbf{L}_{[n]}$  is the Hodge Laplacian and  $\sigma$  is the coupling constant. Since  $\phi$  is taken to be a ( $m$ -dimensional)  $n$ -cochain, as long as  $n > 0$  we need to impose orientation equivariance of the dynamics which implies that only odd functions  $\mathbf{F}$  and  $\mathbf{h}$  can be chosen, although these functions do not have other limitations.

On a network ( $n = 0$ ) it is always possible to observe a globally synchronized dynamical state of Eq. (S-30). A global synchronized state refers to the state in which each oscillator follows the same dynamics, i.e.,  $\phi_\alpha = w(t)$  with  $\dot{w} = F(w)$ . This implies that the topological signal is given by  $\phi = w(t)\mathbf{1}$ . On a (connected) network this dynamical state is always ensured because the constant eigenvector  $\mathbf{1}$  is the unique harmonic eigenvector of the graph Laplacian  $\mathbf{L}_{[0]}$ . Thus the key problem is whether this dynamical state is stable, leading to the Master Stability Function framework [21, 22] to assess whether the global synchronization state is stable. However for higher-order topological signals with  $n > 0$  the constant eigenvector  $\mathbf{1}$  in general is not in the kernel of  $\mathbf{L}_{[n]}$ .

Note that an additional complexity of the problem arises from the fact that for topological signals the synchronized state is a cochain, i.e., it has a sign depending on the orientation of the simplices. This implies that strictly speaking a global synchronized state is proportional to the eigenvector  $\mathbf{u}$  with elements  $|u_i| = 1$ .

It follows that only simplicial or cell complexes admitting  $\mathbf{u}$  in the kernel of the Hodge Laplacian  $\mathbf{L}_{[n]}$  can display global synchronization. Specifically, in order to observe global synchronization we must impose

$$\mathbf{L}_{[n]}\mathbf{u} = \mathbf{0}, \quad (\text{S-31})$$

which due to Hodge decomposition implies

$$\mathbf{L}_{[n]}^{up}\mathbf{u} = \mathbf{0}, \quad \mathbf{L}_{[n]}^{down}\mathbf{u} = \mathbf{0}. \quad (\text{S-32})$$

These are a very restrictive topological conditions, however there are some topologies that allow global synchronization of their topological signals for every dimensions such as the square lattices (2D torus) and cubic lattices (3D torus) with periodic boundary conditions. Other notable examples of simplicial and cell complexes admitting global synchronization of their  $n$ -order topological signals are arbitrary  $n$ -dimensional discrete manifolds.

Interestingly, the theory of Global Topological Synchronization can also exclude the existence of global synchronization in some general scenarios. For instance, while odd-dimensional topological signal can synchronize on cell complexes they can never synchronize on unweighted simplicial complexes of dimension  $d > 1$ .

On topologies on which the global synchronized state exist, it is necessary to also check whether this dynamical state is stable. This is achieved by extending the realm of the Master Stability Function to topological signals (see [20] for details).

### D. Topological synchronization: Supplementary information on Figure 3 and Videos 1-6

#### 1. Topological Kuramoto model

We consider a cell complex formed by two octagons sharing one edge illustrated in Figure S – 4. The Supplementary Videos 1-3 show the visualization of the Topological Kuramoto model for edge topological signals when the two octagons are empty (Video 1), when one is filled and the other is empty (Video 2) and when both are filled (Video 3) each one of them recorded for high values of the coupling constant  $\sigma$ . We note that the Topological Kuramoto model leads to non trivial synchronized dynamics only in presence of harmonic modes. Thus, when both octagons are filled the dynamics freeze.

In the case in which one octagon is filled and one octagon is empty/unfilled it is possible to observe the localization of the synchronized state on the unfilled octagon as revealed by the results shown in Figure 3 of the main text.

To this end we construct a matrix  $\mathbf{H}$  which has as columns the two co-cycles relative to the two octagons of the simplicial complex assumed to be empty. With reference to the labelling shown in Figure S – 4, we define  $\mathbf{H}$  as

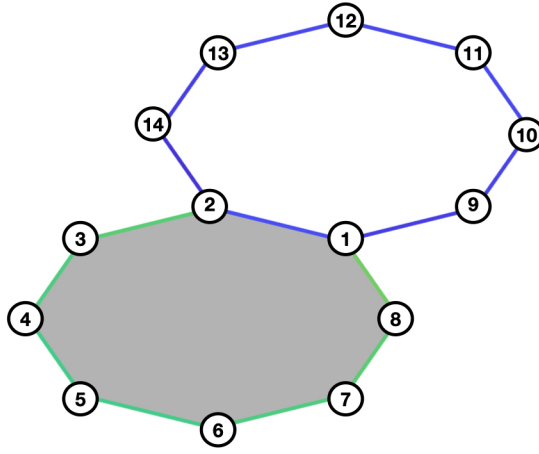


FIG. S-4. **Example of cell complex used to illustrate the Topological Kuramoto model.** Illustration of the cell complex used to illustrate the Topological Kuramoto model in Figure 3 of the main text and in Videos 1-3. Here we indicate explicitly the labelling of the nodes.

$$\mathbf{H} = \begin{array}{c|cc} & h_1 & h_2 \\ \hline [1, 2] & 1 & 1 \\ [2, 3] & 1 & 0 \\ [3, 4] & 1 & 0 \\ [4, 5] & 1 & 0 \\ [5, 6] & 1 & 0 \\ [6, 7] & 1 & 0 \\ [7, 8] & 1 & 0 \\ [1, 8] & -1 & 0 \\ [1, 9] & 0 & -1 \\ [9, 10] & 0 & -1 \\ [10, 11] & 0 & -1 \\ [11, 12] & 0 & -1 \\ [12, 13] & 0 & -1 \\ [13, 14] & 0 & -1 \\ [2, 14] & 0 & 1 \end{array} . \quad (\text{S-33})$$

The two  $m \in 1, 2$  complex local order parameters reported in Figure 3 are defined as

$$X_m = \frac{1}{8} \sum_{\alpha} e^{iH_{\alpha h_m} \phi_{\alpha}} . \quad (\text{S-34})$$

Each of these two complex local order parameters can be used to probe the synchronization along the two octagons. From Figure 3 it is apparent that while the order parameter corresponding to the empty octagon maintains a constant absolute value, which is indicative of a good synchronization behaviour, the one corresponding to the filled octagons does not, demonstrating the localization of the synchronized dynamics on the empty octagon. In the Videos 1-3 and in Figure 3 the intrinsic frequencies are taken to be  $\omega = \omega^{(0)} + \boldsymbol{\eta}$  where  $\omega_{\alpha}^{(0)} = 5(H_{\alpha, h_1} + H_{\alpha, h_2} - H_{\alpha, h_1} H_{\alpha, h_2})$  and  $\boldsymbol{\eta}$  is taken to be a random vector whose elements are drawn from a normal distribution  $\eta_{\alpha} \sim \mathcal{N}(0, 3)$ . The coupling constant  $\sigma$  of the Topological Kuramoto model is taken to be  $\sigma = 25$ .

The code for Topological Kuramoto model is available at the GitHub repository [23].

## 2. Global Topological Synchronization

In order to investigate the Global Topological Synchronization on simplicial and cell complexes we consider the Stuart-Landau model. The Stuart-Landau (SL) model [24–26] is a important model for studying global synchronization because it provides the normal form for a generic system close to a supercritical Hopf-bifurcation and for this



reason it has been largely used in the literature to study synchronization or the Benjamin-Feir instability [27, 28]. This model has been also used to investigate global synchronization of node signals in time varying networks in [29].

In this model the elements of the  $n$  cochain  $\phi$ , are complex valued, i.e.,  $\phi_\alpha = w \in \mathbb{C}$ . The functions  $F(w)$  and  $h(w)$  are taken to be  $F(w) = \delta w - \mu|w|^2 w$ ,  $h(w) = w|w|^{m-1}$  where  $\sigma, \mu \in \mathbb{C}$  and  $m \in \mathbb{N}$  are parameters of the model. Note that these functions are odd, therefore this choice allows us to defined an equivariant dynamical equation for Global Topological Synchronization.

The uncoupled system  $\dot{\phi} = \mathbf{F}(\phi)$  leads to identical uncoupled equations for every simplex that read  $\dot{w} = F(w)$ . This equation admits a limit cycle solution  $w^{LC}(t) = \sqrt{\delta_{\Re}/\mu_{\Re}} e^{i\omega t}$ , where the frequency of the oscillation is given  $\omega = \delta_{\Im} - \mu_{\Im}\delta_{\Re}/\mu_{\Re}$ ; moreover the limit cycle is stable provided  $\delta_{\Re} > 0$  and  $\mu_{\Re} > 0$ , conditions that we hereby assume to hold true.

If the Master Stability Function conditions are satisfied, then global synchronization of topological signals of any dimension can be achieved on  $d$ -dimensional square lattices with boundary conditions.

In Figure 3 we report evidence for Global Topological Synchronization of edge signals on a 2-dimensional cell complex formed by a square lattice tessellation of a torus.

The complex Kuramoto order parameter shown in Figure 3 is taken to be

$$X = \frac{1}{N_n} \sum_{\alpha} \rho_{\alpha} e^{iu_{\alpha}\theta_{\alpha}}, \quad (\text{S-35})$$

where  $(\rho_{\alpha})^2 = (\Re w_{\alpha})^2 + (\Im w_{\alpha})^2$  and  $\theta_{\alpha} = \arg w_{\alpha}$  and  $\mathbf{u}$  is the harmonic eigenvector with elements  $|u_{\alpha}| = 1$  along which the global synchronization takes place. This order parameter on the synchronized state has absolute value  $R = |X| = 1$ .

The Supplementary-Videos (4-6) provide further evidence of Global Topological Synchronization with a visualization of the global synchronization of squares (Video 4), edges (Video 5) and nodes (Video 6) emerging on this cell complex.

The 2-dimensional cell complex is formed by a square lattice tessellation of a torus with  $N_0 = 64$  nodes,  $N_1 = 128$  edges, and  $N_2 = 64$  faces (squares). Figure 3 and the Supplementary Videos 4-6 have been obtained by using the following (generic) values of the parameters

$$\delta = 1.0 + i4.3, \quad \mu = 1.0 + i1.1, \quad \sigma = -1.0 + i0.5, \quad m = 3.$$

The harmonic eigenvector is taken to be  $\mathbf{u} = \mathbf{1}$ .

The code for Global Topological Synchronization is available at the GitHub repository [23].

### III. COUPLED DYNAMICS OF TOPOLOGICAL SIGNALS

#### A. Dirac synchronization

An important question is to define non-linear dynamics of coupled topological signals. To this end, we consider topological signals of nodes and edges coupled with the Dirac operator. Possibly these results can be also extended to higher-dimensional simplicial and cell complexes.

Focusing on the dynamics on a network (i.e., a simplicial complex of dimension  $d = 1$ ), the topological spinor has components  $\Psi = (\theta, \phi)^{\top}$  and the Dirac operator  $\mathbf{D}$  is given by

$$\mathbf{D} = \begin{pmatrix} 0 & \mathbf{B}_{[1]} \\ \mathbf{B}_{[1]}^{\top} & 0 \end{pmatrix}. \quad (\text{S-36})$$

By defining the vector of intrinsic frequencies  $\Omega = (\omega, \hat{\omega})^{\top}$  where  $\omega$  and  $\hat{\omega}$  are the intrinsic frequencies of nodes and edges respectively, we observe that the Topological Kuramoto model on nodes and edges obeys

$$\dot{\Psi} = \Omega - \sigma \mathbf{D} \sin(\mathbf{D}\Psi) \quad (\text{S-37})$$

where the sin function is taken element-wise. This dynamics is the gradient flow of the Hamiltonian function

$$\mathcal{H} = -\Omega^{\top} \Psi - \sigma \mathbf{1}_{N_0+N_1}^{\top} \cos(\mathbf{D}\Psi). \quad (\text{S-38})$$

The linearized version of this dynamics when we approximate  $\sin(x) \simeq x$  becomes

$$\dot{\Psi} = \Omega - \sigma \mathbf{D}^2 \Psi, \quad (\text{S-39})$$

Since  $\mathbf{D}^2 = \mathcal{L}$  has a non-negative spectrum, from this equation it is easy to derive that the equation displays a stable node fixed point for the irrotational component of  $\Psi$  at  $\Psi^{irr} = \Psi - \Psi^{harm}$ .

Dirac synchronization proposes a way to couple the node and edge signal together using the normalized Dirac operator  $\hat{\mathbf{D}}$  that has eigenvalues  $\lambda$  of absolute values less or equal to one. This operator is defined as

$$\hat{\mathbf{D}} = \begin{pmatrix} 0 & \mathbf{K}^{-1}\mathbf{B}_{[1]} \\ \mathbf{B}_{[1]}^\top/2 & 0 \end{pmatrix}, \quad (\text{S-40})$$

and the its square root of the normalized Gauss-Bonnet Laplacian  $\hat{\mathbf{D}}^2 = \hat{\mathcal{L}}$ .

Dirac synchronization[30, 31] couples the node and edge topological signals by introducing a phase lag and defining a non-equilibrium dynamics given by

$$\dot{\Psi} = \Omega - \sigma \hat{\mathbf{D}} \sin((\hat{\mathbf{D}} - z\gamma\hat{\mathcal{L}})\Psi), \quad (\text{S-41})$$

where  $z > 0$ . Note however that, due to the introduction of the phase lag, this dynamics cannot be interpreted anymore as a gradient flow.

The linearized dynamics obeys in this case

$$\dot{\Psi} = \Omega - \sigma((\hat{\mathbf{D}}^2 + z\gamma\hat{\mathcal{L}}^3)\Psi). \quad (\text{S-42})$$

A direct calculation shows that this system of equations displays a stable focus fixed point for the irrotational component of  $\Psi$  at  $\Psi^{irr} = \Psi - \Psi^{harm}$  (see for details [31]).

Dirac synchronization admits two order parameters, each depending on both nodes and edge dynamics, demonstrating the established dependence of the two topological signals.

On fully connected networks and random networks with given degree distribution, Dirac synchronization admits a stable hysteresis loop with either one or two discontinuous transitions depending on the values of  $z$ . The phase diagram is well captured by the annealed network approximation [30, 31].

A notable aspect of Dirac synchronization is that the model displays the emergence of rhythmic phase, i.e., a periodic oscillation of one of the two complex order parameter independently on the intrinsic frequencies.

## B. Topological pattern formation

Topological pattern formation of nodes and edges signal can be obtained by coupling the signals with the Dirac operator. When both nodes and edge topological signals take values on  $\mathbb{R}$  the observed topological patterns are static [32]. However by considering either two nodes signals and one node signal or vice-versa one node signal and two edge signals the patterns can become dynamical under suitable dynamical conditions [10]. Here we outline the theory of topological pattern formation in this latter case.

We assume that the topological spinor of the network  $\Psi = C^0 \oplus C^0 \oplus C^1$  is given by

$$\Psi = \begin{pmatrix} \theta \\ \phi \end{pmatrix}, \quad \text{where} \quad \theta = \begin{pmatrix} u \\ v \end{pmatrix}, \quad \phi = w, \quad (\text{S-43})$$

where  $u \in \mathbb{R}^{N_0}, v \in \mathbb{R}^{N_0}$  and  $w \in \mathbb{R}^{N_1}$ . In other words, we consider two topological node signals and one topological edge signal. In presence of three topological signals on nodes and links we need to define the *three way Dirac operator*  $\mathcal{D}$  that couples the dynamics on the nodes to the dynamics on the edges. The three-way Dirac operator  $\mathcal{D}: C^0 \oplus C^0 \oplus C^1 \rightarrow C^0 \oplus C^0 \oplus C^1$  is defined as

$$\mathcal{D} = \tilde{\gamma}\partial, \quad (\text{S-44})$$

where  $\partial$  is the Hodge Dirac operator that projects the nodes signals into two edge signals and projects the edges signal into one node signal, while the gamma matrix  $\tilde{\gamma}$  compresses the two projected node signals into one edge signal and expands the one projected edge signal into two node signals. Specifically, the Hodge Dirac operator  $\partial: C^0 \oplus C^0 \oplus C^1 \rightarrow C^0 \oplus C^1 \oplus C^1$  is defined as

$$\partial = \begin{pmatrix} \mathbf{0} & \mathbf{I}_1 \otimes \mathbf{B}_{[1]} \\ \mathbf{I}_2 \otimes \mathbf{B}_{[1]}^\top & \mathbf{0} \end{pmatrix}, \quad \text{or,} \quad \partial = \begin{pmatrix} 0 & 0 & \mathbf{B}_{[1]} \\ \mathbf{B}_{[1]}^\top & 0 & 0 \\ 0 & \mathbf{B}_{[1]}^\top & 0 \end{pmatrix}. \quad (\text{S-45})$$

The gamma matrix  $\tilde{\gamma} : C^0 \oplus C^1 \oplus C^1 \rightarrow C^0 \oplus C^0 \oplus C^1$  is defined in terms of 2-dimensional column vector  $\alpha = (\alpha_u, \alpha_v)^\top$  and a 2-dimensional row vector  $\beta = (\beta_u, \beta_v)$ , as

$$\tilde{\gamma} = \begin{pmatrix} \alpha \otimes \mathbf{I}_{N_0} & \mathbf{0} \\ \mathbf{0} & \beta \otimes \mathbf{I}_{N_1} \end{pmatrix}, \quad \text{or} \quad \tilde{\gamma} = \begin{pmatrix} \alpha_u \mathbf{I}_{N_0} & 0 & 0 \\ \alpha_v \mathbf{I}_{N_0} & 0 & 0 \\ 0 & \beta_u \mathbf{I}_{N_1} & \beta_v \mathbf{I}_{N_1} \end{pmatrix}. \quad (\text{S-46})$$

It follows that the three-way Dirac operator can be also expressed as

$$\mathcal{P} = \tilde{\gamma} \partial = \begin{pmatrix} 0 & 0 & \alpha_u \mathbf{B}_{[1]} \\ 0 & 0 & \alpha_v \mathbf{B}_{[1]} \\ \beta_u \mathbf{B}^\top & \beta_v \mathbf{B}_{[1]}^\top & 0 \end{pmatrix} \quad \text{with} \quad \mathcal{P}^2 = \tilde{\mathcal{L}} = \begin{pmatrix} D_{uu} \mathbf{L}_{[0]} & D_{uv} \mathbf{L}_{[0]} & 0 \\ D_{vu} \mathbf{L}_{[0]} & D_{vv} \mathbf{L}_{[0]} & 0 \\ 0 & 0 & D_{ww} \mathbf{L}_{[1]} \end{pmatrix}, \quad (\text{S-47})$$

with  $D_{uu} = \alpha_u \beta_u$ ,  $D_{uv} = \alpha_u \beta_v$ ,  $D_{vu} = \alpha_v \beta_u$ ,  $D_{vv} = \alpha_v \beta_v$  and  $D_{ww} = \alpha_u \beta_u + \alpha_v \beta_v$ , assumed to be non-negative.

Let us consider the uncoupled dynamics

$$\dot{\Psi} = \mathbf{F}(\Psi, \partial \Psi), \quad (\text{S-48})$$

where the function  $\mathbf{F}$  is taken element-wise. Topological pattern formation emerges when a uniform solution to the dynamical system in Eq. (S-48) becomes unstable in presence of a coupling among the different simplices induced through the Gauss-Bonnet Laplacian or the three way Dirac operator. Thus Topological Pattern Formation is described by the following dynamical model

$$\dot{\Psi} = \mathbf{F}(\Psi, \partial \Psi) - c_1 \mathcal{P} \Psi - c_2 \tilde{\mathcal{L}} \Psi, \quad (\text{S-49})$$

where  $c_1 \in \mathbb{R}$ ,  $c_2 \in \mathbb{R}^+$ . This equation can be rewritten as

$$\begin{cases} \dot{u} = f(u, v, \mathbf{B}_{[1]} w) - c_2 \mathbf{L}_{[0]} (D_{uu} u + D_{uv} v) - c_1 \alpha_u \mathbf{B} w, \\ \dot{v} = g(u, v, \mathbf{B}_{[1]} w) - c_2 \mathbf{L}_{[0]} (D_{vu} u + D_{vv} v) - c_1 \alpha_v \mathbf{B} w, \\ \dot{w} = h(\mathbf{B}_{[1]}^\top u, \mathbf{B}_{[1]}^\top v, w) - c_2 D_{ww} \mathbf{L}_{[1]} - c_1 \mathbf{B}_{[1]}^\top (\beta_u u + \beta_v v). \end{cases} \quad (\text{S-50})$$

Under suitable dynamical conditions, the homogeneous solution of the uncoupled dynamics becomes unstable leading to topological static or dynamical patterns (see for details [10]). When  $c_2 > 0$  the topological patterns on nodes and edges that can emerge are driven by the diffusion dynamics are called *Topological Turing patterns*. When  $c_2 = 0$  and  $c_1 \neq 0$  the observed topological patterns that can emerge are exclusively driven by the Dirac operator and are called *Topological Dirac patterns*.

### C. Topological pattern formation: Supplementary information on Supplementary Videos 7-8

We illustrate the emergence of dynamical Topological Turing and Dirac patterns [10] in the Supplementary Videos 7-8. The model considers two topological signals on the nodes ( $u$  and  $v$ ) and two topological signals on the edges and a specific choice of the functions  $f, g, h$  defined in Eq. (S-50) given by

$$\begin{cases} f(u, v, \mathbf{B}_{[1]} w) = \sigma_1 u - \eta_1 u^3 + \xi_1 v + \zeta_1 \mathbf{B}_{[1]} w, \\ g(u, v, \mathbf{B}_{[1]} w) = \sigma_2 v + \xi_2 u + \zeta_2 \mathbf{B}_{[1]} w, \\ h(\mathbf{B}_{[1]}^\top u, \mathbf{B}_{[1]}^\top v, w) = \sigma_3 w + \zeta_3 \mathbf{B}_{[1]}^\top u + \zeta_4 \mathbf{B}_{[1]}^\top v. \end{cases}$$

The homogeneous equilibrium state is given by  $(0, 0, 0)$ .

Both Videos display the dynamics of one of the two topological signals on the nodes (species  $u$ ), and of the edge topological signals  $w$ , on a benchmark network of 12 nodes and 16 edges.

Video 7 shows the case of dynamics Turing patterns, which are driven by diffusion ( $c_2 > 0$ ) and are strongly dependent on the initial perturbation, while in Video 8 we show the Dirac pattern occurring when no diffusion takes place (i.e.,  $c_2 = 0$ ) and the patterns are solely induced by the Dirac operator. The latter Dirac patterns exhibit a shorter transient and the asymptotic attractor, not only is more regular when compared to the Turing one, but it also does not depend on the initial perturbations, i.e., Dirac patterns are robust. For both Videos the initial perturbation of the homogeneous equilibrium is the order of  $10^{-2}$ . The parameters for Video 7 are  $\sigma_1 = 1$ ,  $\sigma_2 = -1.4$ ,  $\eta_1 = -3$ ,  $\xi_1 = -0.5$ ,  $\xi_2 = 5$ ,  $\zeta_1 = 0.1$ ,  $\zeta_2 = 6$ ,  $\zeta_3 = 6$ ,  $\zeta_4 = 1$ ,  $c_1 = -1$ ,  $c_2 = 1$ ,  $\alpha_u = 1$ ,  $\alpha_v = 1$ ,  $\beta_u = 1$ ,  $\beta_v = 0.1$ ; those for Video 8 are the same except for  $c_2 = 0$  and  $\sigma_3 = -10$ .

The code for Dirac Pattern Formation is available at the GitHub repository [23].

## IV. TOPOLOGICAL SIGNAL PROCESSING

Real and noisy topological signal data can be processed using signal processing methods using algebraic topology operators such as the Hodge Laplacians and the Dirac operator. In this section we provide a brief overview of this rapidly emerging field [33–35].

### A. Hodge Laplacian signal processing

Hodge Laplacian signal processing [33, 34] refers to signal processing algorithms using the Hodge Laplacian to reconstruct a true topological signal starting from noisy data.

Let us consider a true topological signal  $\mathbf{s} \in C^n$  and a noisy signal  $\tilde{\mathbf{s}} = \mathbf{s} + \boldsymbol{\epsilon}$  where  $\boldsymbol{\epsilon}$  is a noisy signal whose elements are drawn independently from a given distribution, typically chosen to be a normal distribution.

We assume that we have access only to the noisy signal  $\tilde{\mathbf{s}}$  and that our goal is to generate a reconstructed signal  $\hat{\mathbf{s}}$  that filters out the noise and is actually close to the true signal  $\mathbf{s}$ . This reconstruction is achieved under certain hypotheses on the nature of the true signal. Specifically in Hodge-Laplacian signal processing it is assumed that the true signal is formed by low eigenvectors of the Hodge Laplacian  $\mathbf{L}_{[n]}$ . Thus, the reconstructed signal  $\hat{\mathbf{s}}$  minimizes the loss function  $\mathcal{F}$  given by

$$\mathcal{F} = \|\hat{\mathbf{s}} - \tilde{\mathbf{s}}\|^2 + \tau \hat{\mathbf{s}}^\top \mathbf{L}_{[n]} \hat{\mathbf{s}}. \quad (\text{S-51})$$

This loss function includes two terms: the first term keeps the reconstructed signal close to the (noisy) data, the second term (or regularization term) enforces a cost to the modes of the reconstructed signal corresponding to high eigenvalues of the Hodge Laplacian. From this minimization problem it follows that the reconstructed signal is given by

$$\hat{\mathbf{s}} = [\mathbf{I}_{N_n} + \tau \mathbf{L}_{[n]}]^{-1} \tilde{\mathbf{s}}. \quad (\text{S-52})$$

It follows that this reconstructed signal leaves the harmonic component of the topological signal unchanged while it filters out the higher modes of the irrotational and solenoidal components of the topological signal.

### B. Dirac signal processing

The Hodge Laplacian signal processing works efficiently to filter noisy data of topological signals defined on simplices of dimension  $n \geq 0$ . However the Hodge Laplacian signal processing filters signal of different dimensions independently while in general the data can be formed by topological signals of different dimensions. For instance in a simplicial complex of dimension  $d = 2$ , we might have access simultaneously to (noisy) topological signals on the nodes  $\tilde{\mathbf{s}}_{[0]}$ , on the edges  $\tilde{\mathbf{s}}_{[1]}$  and on the triangles  $\tilde{\mathbf{s}}_{[2]}$ .

In order to *jointly* filter topological signals of different dimensions we cannot use the Hodge Laplacians or the block diagonal Gauss-Bonnet Laplacian. Thus, to address this problem, Dirac signal processing harnesses the power of processing topological signals with the Dirac operator.

The noisy signals  $\tilde{\mathbf{s}}_{[n]}$  are assumed to be related to the true signals  $\mathbf{s}_{[n]}$  by  $\tilde{\mathbf{s}}_{[n]} = \mathbf{s}_{[n]} + \boldsymbol{\epsilon}_{[n]}$ , where  $\boldsymbol{\epsilon}_{[n]}$  are vectors whose elements are independently drawn from a random distribution, typically taken to be a normal distribution. Let us then consider the topological spinors  $\mathbf{S}, \tilde{\mathbf{S}}$  and  $\hat{\mathbf{S}}$  describing for the entire simplicial complex true signal, noisy signal and reconstructed signal respectively, i.e.,

$$\mathbf{S} = \begin{pmatrix} \mathbf{s}_{[0]} \\ \mathbf{s}_{[1]} \\ \mathbf{s}_{[2]} \end{pmatrix}, \quad \tilde{\mathbf{S}} = \begin{pmatrix} \tilde{\mathbf{s}}_{[0]} \\ \tilde{\mathbf{s}}_{[1]} \\ \tilde{\mathbf{s}}_{[2]} \end{pmatrix}, \quad \hat{\mathbf{S}} = \begin{pmatrix} \hat{\mathbf{s}}_{[0]} \\ \hat{\mathbf{s}}_{[1]} \\ \hat{\mathbf{s}}_{[2]} \end{pmatrix}. \quad (\text{S-53})$$

In order to jointly filter the signals Dirac signal processing proceed by minimizing the loss function

$$\mathcal{F} = \|\hat{\mathbf{S}} - \tilde{\mathbf{S}}\|^2 + \tau \hat{\mathbf{S}}^\top (\mathbf{D}_{[1]} - m_{[1]} \mathcal{I}_{[1]})^2 \hat{\mathbf{S}} + \tau \hat{\mathbf{S}}^\top (\mathbf{D}_{[2]} - m_{[2]} \mathcal{I}_{[2]})^2 \hat{\mathbf{S}}, \quad (\text{S-54})$$

where the Dirac matrices  $\mathbf{D}_{[r]}$  are defined in Eq.(S-14) and the matrices  $\mathcal{I}_{[r]}$  with  $r \in \{1, 2\}$  are given by

$$\mathcal{I}_{[1]} = \begin{pmatrix} \mathbf{I}_{N_0} & 0 & 0 \\ 0 & \mathbf{I}_{N_1} & 0 \\ 0 & 0 & 0 \end{pmatrix}, \quad \mathcal{I}_{[2]} = \begin{pmatrix} 0 & 0 & 0 \\ 0 & \mathbf{I}_{N_1} & 0 \\ 0 & 0 & \mathbf{I}_{N_2} \end{pmatrix}. \quad (\text{S-55})$$

Due to Dirac decomposition, we can uniquely decompose the data  $\mathbf{S}$  as

$$\mathbf{S} = \mathbf{S}_{[1]} + \mathbf{S}_{[2]} + \mathbf{S}_{\text{harm}} \quad (\text{S-56})$$

where  $\mathbf{S}_{[r]} \in \text{im}(\mathbf{D}_{[r]})$ , and  $\mathbf{S}_{\text{harm}} \in \ker(\mathbf{D}_{[1]} + \mathbf{D}_{[2]})$ . A similar decomposition applies for the measured ( $\tilde{\mathbf{S}}$ ) and for the reconstructed ( $\hat{\mathbf{S}}$ ) signals.

The underlying hypothesis of Dirac signal processing is that the true signal has zero harmonic component  $\mathbf{S}_{\text{harm}} = \mathbf{0}$  and that each  $\mathbf{S}_{[r]}$  is aligned along an eigenvector corresponding to a non-zero eigenvalue of the Dirac operator  $\mathbf{D}_{[r]}$ .

Thus filtering out the harmonic component and assuming  $\mathbf{S}_{\text{harm}} = \hat{\mathbf{S}}_{\text{harm}} = \tilde{\mathbf{S}}_{\text{harm}} = \mathbf{0}$ , Dirac signal processing reduces to the problem of minimizing the two loss functions

$$\mathcal{F}_{[r]} = \|\hat{\mathbf{S}}_{[r]} - \tilde{\mathbf{S}}_{[r]}\|^2 + \tau \hat{\mathbf{S}}_{[r]}^\top (\mathbf{D}_{[r]} - m_{[r]} \mathcal{I}_{[r]})^2 \hat{\mathbf{S}}_{[r]}, \quad (\text{S-57})$$

with  $r \in \{1, 2\}$ . This loss function is formed by two terms: the first term minimizes the distance between the measured and reconstructed signal, the second term (the regularization term) enforces some cost associated to the eigenmodes corresponding on eigenvalues departing from  $m_{[r]}$ .

Note that one of the characteristic of Dirac signal processing is that  $m_{[r]}$  are learnable parameters, thus the loss function  $\mathcal{F}_{[r]}$  should be minimized with respect to the reconstructed signal  $\hat{\mathbf{S}}_{[r]}$  and the parameter  $m_{[r]}$  as well.

The Dirac algorithm is iterative: first  $\mathcal{F}_{[r]}$  is optimized with respect to  $\hat{\mathbf{S}}_{[r]}$  keeping  $m_{[r]}$  fixed, then  $m_{[r]}$  is updated in order to minimize  $\mathcal{F}$  for fixed  $\hat{\mathbf{S}}_{[r]}$ .

Thus starting from an initial guess for  $m_{[r]}$  given by  $m_{[r]}^{(0)}$  the algorithm proceeds by iterating for every  $t > 0$  and until convergence of the iteration with a preset tolerance level, the map

$$\begin{aligned} \hat{\mathbf{S}}_{[r]}^{(t)} &= \left[ \mathcal{I}_{[r]} + \tau \left( \mathbf{D}_{[r]} - m_{[r]}^{(t-1)} \mathcal{I}_{[r]} \right)^2 \right]^{-1} \tilde{\mathbf{S}}_{[r]} \\ m_{[r]}^{(t)} &= (1 - \eta) m_{[r]}^{(t-1)} + \eta \frac{(\hat{\mathbf{S}}_{[r]}^{(t)})^\top \mathbf{D}_{[r]} \hat{\mathbf{S}}_{[r]}^{(t)}}{(\hat{\mathbf{S}}_{[r]}^{(t)})^\top \hat{\mathbf{S}}_{[r]}^{(t)}}, \end{aligned} \quad (\text{S-58})$$

where  $\eta < 1$  is a small auxiliary parameter. Provided that the initial guess  $m_{[r]}^{(0)}$  is not too far from the eigenvalue of the true signal, this algorithm has been shown to have good performance on synthetic data. On real data also it is observed that the model can outperform Hodge Laplacian signal processing obtained when  $m_{[r]}$  is set equal to zero. For details we refer the reader to Ref. [31].

The code for Dirac signal processing is available at the GitHub repository [23].

## V. TOPOLOGY IS DYNAMICAL

### A. Triadic percolation

Triadic interactions are higher-order interactions between nodes and structural edges that can be key to modulating the interaction strength or even the existence of structural edges. Thus triadic interactions can be used to describe the dynamical changes of the topology of a network. This is achieved in the framework of triadic percolation [36, 37] in which triadic interactions are used to regulate up or down the edges of a network.

A network with triadic interactions can be seen as a network of networks formed by a structural network,  $G = (V, E)$  of nodes in  $V$  connected by structural edges in  $E$  and a bipartite network  $\mathcal{G} = (V, E, \mathcal{E})$  whose edges in  $\mathcal{E}$  connect nodes in  $V$  and structural edges on  $E$ . The network  $\mathcal{G}$  is signed since regulatory triadic interactions can both enhance or inhibit the interactions between other nodes. For instance, in ecosystems [38], a species can either enhance or inhibit the interactions between other two species. We say that a node is a positive/negative regulator of a structural edge if its interaction is positive/negative. Note that a node can be at the same time a positive regulator of a given structural edge and a negative regulator of another structural edge.

Triadic percolation considers a two-step process in which structural interactions determine which nodes are active, while triadic regulatory interactions determine which edges are active. In particular, the triadic percolation algorithm involves two steps performed iteratively after an initial condition.

- *Step 1:* Given the set of active edges, nodes are active if they belong to the giant component of the network.

- *Step 2:* Edges are inactive if none of the positive regulator nodes is active or if at least one of the negative regulator nodes is active, otherwise nodes are active with probability  $p$ .

Assuming that the structural network is a random uncorrelated network with degree distribution  $P(k)$ , and that the regulatory network is a Poisson network in which each edge has an average number of positive and negative regulatory interactions given by  $c_+$  and  $c_-$  respectively, the equations for triadic percolation can be derived analytically. The fraction of nodes  $R(t)$  that at time  $t$  are in the giant component are given by

$$R^{(t)} = 1 - G_0 \left( 1 - S^{(t)} p_L^{(t-1)} \right), \quad (\text{S-59})$$

where  $S(t)$  indicates the probability that at time  $t$  a random edge leads to a node in the giant component, and  $p_L(t)$  is the probability that the edges are active, each obeying

$$\begin{aligned} S^{(t)} &= 1 - G_1 \left( 1 - S^{(t)} p_L^{(t-1)} \right), \\ p_L^{(t)} &= p e^{-c_- R^{(t)}} \left( 1 - e^{-c_+ R^{(t)}} \right). \end{aligned} \quad (\text{S-60})$$

These equations are expressed in terms of the generating functions given by

$$G_0(x) = \sum_k \pi(k) x^k, \quad G_1(x) = \sum_k \pi(k) \frac{k}{\langle k \rangle} x^{k-1}. \quad (\text{S-61})$$

The equations for triadic percolation can be formally written as the map:

$$R^{(t)} = f \left( p_L^{(t-1)} \right), \quad p_L^{(t)} = g \left( R^{(t)} \right). \quad (\text{S-62})$$

This map can be shown to undergo a route to chaos in the universality class of the logistic map. In particular, the order parameter  $R(t)$  of triadic percolation can either display periodic oscillations or in the thermodynamic limit chaotic behavior. In correspondence of period two oscillations, the number of active nodes oscillates periodically and we say that the network displays a *blinking* behavior. Interestingly, in absence of negative interactions the dynamics of triadic percolation always reach a static steady state. However, the phase diagram can remain interesting and can to display a discontinuous hybrid transition [36].

On spatial networks, it can be shown that not only the fraction of active nodes changes dynamically on time but also the topology of the giant component can be strongly non-stationary [17]. In particular, on a spatial network with local structural and regulatory interactions defined on a torus with periodic boundary conditions, triadic percolation leads to giant components that display important topological differences as a function of time.

## B. Triadic percolation: Supplementary information on Figure 4 and Videos 9-10

Figure 4 shows the structure of networks with triadic interactions and the drastic difference between percolation on simple networks and networks with triadic interactions. Panel (c) shows the theoretical result of ordinary percolation of a scale-free network with a degree exponent  $\gamma = 2.5$ , minimum degree  $m = 4$ , and maximum degree  $K = 100$ . Panel (d) displays the percolation on a network with triadic interaction formed by the same scale-free structural network and the regulatory network is Poisson with  $c_+ = 10$  and  $c_- = 2.8$ . Panel (e) shows the chaotic time series in Panel (d) at  $p = 0.8$ .

We illustrate the blinking and chaotic behavior of the number of active nodes in Video 9 and Video 10 respectively. In Video 9, we simulate the triadic percolation on a 100-node network formed by a Poisson structural network with an average degree  $c = 6$  and a Poisson regulatory network with  $c_- = 2$ . The regulatory network is formed exclusively by negative regulations and positive regulations are not required to activate a link. The probability of retaining a link after the regulation is set as  $p = 1$ . In Video 10, the network is formed by the same structural network and a Poisson regulatory network with  $c_+ = 3$  and  $c_- = 2$ . The probability of retaining a link after the regulation is set as  $p = 0.85$ .

The code for triadic percolation is available at the GitHub repository [23].

- [2] B. Eckmann, *Commentarii Mathematici Helvetici* **17**, 240 (1944).
- [3] A. Hatcher, *Algebraic topology* (Cambridge University Press, 2001).
- [4] L. J. Grady and J. R. Polimeni, *Discrete calculus: Applied analysis on graphs for computational science*, Vol. 3 (Springer, 2010).
- [5] F. Baccini, F. Geraci, and G. Bianconi, *Physical Review E* **106**, 034319 (2022).
- [6] G. Bianconi, *J. phys. Complex.* **2**, 035022 (2021).
- [7] S. Lloyd, S. Garnerone, and P. Zanardi, *Nature Communications* **7**, 10138 (2016).
- [8] O. Post, in *Annales Henri Poincaré*, Vol. 10 (Springer, 2009) pp. 823–866.
- [9] S. Krishnagopal and G. Bianconi, *Chaos, Solitons & Fractals* **177**, 114296 (2023).
- [10] R. Muolo, T. Carletti, and G. Bianconi, *Chaos, Solitons & Fractals* **178**, 114312 (2024).
- [11] A. Muhammad and M. Egerstedt, in *Proc. of 17th International Symposium on Mathematical Theory of Networks and Systems* (Citeseer, 2006) pp. 1024–1038.
- [12] J. J. Torres and G. Bianconi, *Journal of Physics: Complexity* **1**, 015002 (2020).
- [13] D. Taylor, F. Klimm, H. A. Harrington, M. Kramár, K. Mischaikow, M. A. Porter, and P. J. Mucha, *Nature Communications* **6**, 7723 (2015).
- [14] Y. Kuramoto, in *International Symposium on Mathematical Problems in Theoretical Physics*, edited by H. Araki (Springer Berlin Heidelberg, Berlin, Heidelberg, 1975) pp. 420–422.
- [15] A. Arnaudon, R. L. Peach, G. Petri, and P. Expert, *Communications Physics* **5**, 211 (2022).
- [16] J. M. Kosterlitz, *Reports on Progress in Physics* **79**, 026001 (2016).
- [17] A. P. Millán, J. J. Torres, and G. Bianconi, *Physical Review Letters* **124**, 218301 (2020).
- [18] R. Ghorbanchian, J. G. Restrepo, J. J. Torres, and G. Bianconi, *Communications Physics* **4**, 120 (2021).
- [19] L. DeVille, *Chaos: An Interdisciplinary Journal of Nonlinear Science* **31**, 023137 (2021).
- [20] T. Carletti, L. Giambagli, and G. Bianconi, *Physical Review Letters* **130**, 187401 (2023).
- [21] H. Fujisaka and T. Yamada, *Progress of Theoretical Physics* **69**, 32 (1983).
- [22] L. M. Pecora and T. L. Carroll, *Physical Review Letters* **80**, 2109 (1998).
- [23] “Github repository: Topology shapes dynamics,” (2024), <https://github.com/Jamba15/TopologyShapesDynamics>.
- [24] A. van Harten, *J. Nonlinear Sci.* **1**, 397 (1991).
- [25] I. Aranson and L. Kramer, *Reviews of Modern Physics* **74**, 99 (2002).
- [26] V. Garca-Morales and K. Krischer, *Contem. Phys.* **53**, 79 (2012).
- [27] H. Nakao, *The European Physical Journal Special Topics* **223**, 2411 (2014).
- [28] F. Di Patti, D. Fanelli, F. Miele, and T. Carletti, *Chaos, Solitons & Fractals* **96**, 8 (2017).
- [29] T. Carletti and D. Fanelli, *Chaos, Solitons & Fractals* **159**, 112180 (2022).
- [30] L. Calmon, J. G. Restrepo, J. J. Torres, and G. Bianconi, *Communications Physics* **5**, 253 (2022).
- [31] L. Calmon, S. Krishnagopal, and G. Bianconi, *Chaos: An Interdisciplinary Journal of Nonlinear Science* **33**, 033117 (2023).
- [32] L. Giambagli, L. Calmon, R. Muolo, T. Carletti, and G. Bianconi, *Physical Review E* **106**, 064314 (2022).
- [33] S. Barbarossa and S. Sardellitti, *IEEE Transactions on Signal Processing* **68**, 2992 (2020).
- [34] M. T. Schaub, Y. Zhu, J.-B. Seby, T. M. Roddenberry, and S. Segarra, *Signal Processing* **187**, 108149 (2021).
- [35] L. Calmon, M. T. Schaub, and G. Bianconi, *New J. Phys.* **25**, 093013 (2023).
- [36] H. Sun, F. Radicchi, J. Kurths, and G. Bianconi, *Nature Communications* **14**, 1308 (2023).
- [37] A. P. Millán, H. Sun, J. J. Torres, and G. Bianconi, *PNAS Nexus*, pgae270 (2024).
- [38] J. Grilli, G. Barabás, M. J. Michalska-Smith, and S. Allesina, *Nature* **548**, 210 (2017).